J Physiol 589.17 (2011) pp 4365–4381

The Journal of Physiology

Enhanced high-frequency membrane potential fluctuations control spike output in striatal fast-spiking interneurones *in vivo*

Jan M. Schulz[1,2], Toni L. Pitcher[1], Shakuntala Savanthrapadian[1], Jeffery R. Wickens[3], Manfred J. Oswald[1] and John N. J. Reynolds[1]

[1] *Department of Anatomy and Structural Biology, School of Medical Sciences, Brain Health Research Centre, University of Otago, PO Box 913, Dunedin 9054, New Zealand*

[2] *Department of Physiology, University of Bern, Bühlplatz 5, 3012 Bern, Switzerland*

[3] *Okinawa Institute of Science and Technology, Uruma, Okinawa 904-2234, Japan*

Non-technical Summary Rhythmic activity patterns are a common theme throughout neuroscience. However, it is still poorly understood how network functions are modulated by fast oscillatory inputs from distant brain regions. In this respect, the striatum is particularly interesting as almost all neuronal activity is driven by long-range inputs. We find that the three main classes of neurones in the striatum show very distinct oscillatory activity patterns in specific frequency ranges. In particular, we show that fast-spiking interneurones are highly sensitive to fast fluctuating synaptic inputs in the intact brain. This sensitivity was probably due to a combination of faster dynamics of synaptic inputs and intrinsic amplification of high-frequency signals. In contrast, projection neurones and other interneurones lacking these mechanisms were insensitive to fast oscillatory input patterns. These results suggest that transmission of fast cortical oscillatory inputs modulates information processing in the striatum via engagement of fast-spiking interneurones.

Abstract Fast-spiking interneurones (FSIs) constitute a prominent part of the inhibitory microcircuitry of the striatum; however, little is known about their recruitment by synaptic inputs in *vivo*. Here, we report that, in contrast to cholinergic interneurones (CINs), FSIs ($n = 9$) recorded in urethane-anaesthetized rats exhibit Down-to-Up state transitions very similar to spiny projection neurones (SPNs). Compared to SPNs, the FSI Up state membrane potential was noisier and power spectra exhibited significantly larger power at frequencies in the gamma range (55–95 Hz). The membrane potential exhibited short and steep trajectories preceding spontaneous spike discharge, suggesting that fast input components controlled spike output in FSIs. Spontaneous spike data contained a high proportion ($43.6 \pm 32.8\%$) of small inter-spike intervals (ISIs) of <30 ms, setting FSIs clearly apart from SPNs and CINs. Cortical-evoked inputs had slower dynamics in SPNs than FSIs, and repetitive stimulation entrained SPN spike output only if the stimulation was delivered at an intermediate frequency (20 Hz), but not at a high frequency (100 Hz). Pharmacological induction of an activated ECoG state, known to promote rapid FSI spiking, mildly increased the power (by $43 \pm 55\%$, $n = 13$) at gamma frequencies in the membrane potential of SPNs, but resulted in few small ISIs (<30 ms; $4.3 \pm 6.4\%$, $n = 8$). The gamma frequency content did not change in CINs ($n = 8$). These results indicate that FSIs are uniquely responsive to high-frequency input sequences. By controlling the spike output of SPNs, FSIs could serve gating of top-down signals and long-range synchronisation of gamma-oscillations during behaviour.

(Received 27 May 2011; accepted after revision 6 July 2011; first published online 11 July 2011)

Corresponding author J. M. Schulz: Department of Physiology, University of Bern, Bühlplatz 5, 3012 Bern, Switzerland. Email: schulz@pyl.unibe.ch

Abbreviations AP, anterior-posterior from bregma; BIC, (–)-bicuculline methochloride; CIN, cholinergic interneurone; CV2, coefficient of variation 2; FSI, fast-spiking interneurone; HFS, high-frequency stimulation; ISI, interspike interval; ML, medio-lateral from midline; ECoG, electro-corticogram; PSP, postsynaptic potential; SPN, spiny projection neurone.

DOI: 10.1113/jphysiol.2011.212944

Introduction

The striatum, the major input nucleus of the basal ganglia, is numerically dominated by a single class of principal neurones, the GABAergic spiny projection neurone (SPN) (Oorschot, 1996). These neurones receive most of the excitatory inputs from cortex and thalamus, provide all output to other basal ganglia nuclei and possess a dense plexus of axon collaterals within the striatum that target neighbouring SPNs. In addition, there are several classes of sparsely distributed interneurones, principally the cholinergic interneurone (CIN), that exhibits prominent responses to subcortical sensory inputs (Schulz *et al.* 2011), and the GABAergic fast-spiking interneurone (FSI). A major challenge in modern systems neuroscience is to understand how synaptic control of interneurone spiking contributes to their functions *in vivo*.

Fast-spiking interneurones are soma-targeting inhibitory neurones and have a common developmental origin in the medial ganglionic eminences in the ventral telencephalic ventricular zone, from where they migrate to their respective target areas (Wonders & Anderson, 2006). Functionally, FSIs of cortex and hippocampus mediate feed-forward and feedback inhibition, and have been implicated in the generation of fast oscillatory neural activity (Bartos *et al.* 2007; Wang, 2010). In the striatum, individual FSIs have a powerful effect on SPN firing (Koos & Tepper, 1999; Mallet *et al.* 2005), whereas neighbouring SPNs do not appear to have the same impact (Tunstall *et al.* 2002). Experimental and computational studies show that feed-forward inhibition could be a potential mechanism of fast gating of afferent inputs (Pouille & Scanziani, 2001; Kremkow *et al.* 2010). Studies on the connectivity between FSIs and SPNs have yielded conflicting results, with one study indicating that FSIs preferentially target SPNs of the direct pathway (Gittis *et al.* 2010), and another finding no differences between direct and indirect pathway SPNs (Planert *et al.* 2010). Thus, it is unclear whether a general gating mechanism exists or alternatively whether FSIs regulate the balance between direct and indirect SPN pathways. In extracellular recording studies in anaesthetized and awake rats, FSIs were shown to be entrained to local and cortical fast gamma oscillations (Berke, 2009; Sharott *et al.* 2009). These observations indicate that FSIs may play a role in gating of cortico-striatal inputs and/or the long-range synchronisation of striatal neurones with their afferent networks.

Despite suggestions that FSIs as a population control the functional state of striatal networks, the activity patterns vary greatly across individual striatal FSIs during behavioural tasks (Berke, 2008; Berke *et al.* 2004). A clearer view of FSI function requires a better understanding of the underlying membrane potential dynamics of FSI spiking *in vivo*. Here, we report the first comprehensive intracellular recording study of FSIs in the adult urethane-anaesthetized rat. We provide a systematic comparison of these recordings with those from another interneurone class (CINs) and SPNs. The results show that the high-frequency signal from the afferent synaptic inputs is strongly enhanced in FSIs and controls their spike output.

Methods

All experiments were performed in accordance with approvals granted by the University of Otago Animal Ethics Committee.

Surgery

Male Wistar, Long-Evans and spontaneously hypertensive (SHR) rats (230–410 g, total $n = 88$) from a number of different studies performed over 11 years (Reynolds & Wickens, 2000; Pitcher *et al.* 2007; Schulz *et al.* 2009, 2010) were anaesthetized with urethane (1.4–1.9 g kg^{-1} I.P.; Biolab Ltd., Auckland, New Zealand), supplemented with additional urethane (0.2 g kg^{-1}) hourly to two-hourly, as required. The core temperature was maintained at 36°C by a homoeothermic blanket. All wounds and pressure points were infiltrated with a long-acting local anaesthetic (bupivacaine, 0.5%). The head was fixed in a stereotaxic frame and surgery was performed as previously described (Schulz *et al.* 2009, 2010). Briefly, a hole was drilled into the skull above the left cortex and a silver wire electrode placed in contact with the dura and secured with dental cement to record the electrocorticogram (ECoG). In the majority of experiments, another hole was drilled above the left SC, around 6.5 mm posterior to bregma (AP −6.5) and 1.4 mm mediolateral from the midline (ML +1.4), for the drug-ejection pipette (Schulz *et al.* 2009, 2010). The pipette and electrode were lowered 4.1 mm from brain surface into the SC deep layers and secured in place with dental cement. Above the right motor cortex, a hole was drilled around AP +2.0/ ML −1.8 to accept concentric electrodes (NEX-100, Rhodes, USA). Stimulating electrodes were secured in place at a depth of 1.8–2 mm. A craniotomy from AP −2.0 to +2.5 and ML +0.5 to +4.0 was made to provide access to the left medial striatum.

Intracellular recordings

Intracellular records were made using micropipettes pulled from 3.0 mm diameter glass (Harvard Apparatus, UK) filled with 1 M potassium acetate (60–100 MΩ resistance), and in some cases containing 2% biocytin. The micropipette was advanced through the striatum

from initial penetrations from AP −0.8 to +1.6 and ML +2.0 to +4.0, until a stable recording (>10 min) was obtained from a striatal neurone. All electrophysiologically identified SPNs exhibited (i) fluctuations of >7 mV in amplitude between a hyperpolarised Down state and a depolarised Up state, (ii) a Down state membrane potential more negative than −70 mV, (iii) a slow ramp-like depolarisation in response to a just suprathreshold current pulse (see Fig. 1), and (iv) action potential amplitudes greater than 50 mV, as is typical for these neurones (Reynolds & Wickens, 2000; Mahon *et al.* 2001; Schulz *et al.* 2009, 2010). All putative interneurones were accepted as long as they exhibited a sufficiently polarised membrane potential (<−50 mV) and maintained a stable current–voltage relationship (i.e. that did not change over >10 min). Current–voltage relations were obtained by injecting hyperpolarising and depolarising current pulses through the micropipette during the neurone's Down state (Fig. 1), using an Axoclamp-2B amplifier (Axon Instruments Inc., Union City, CA, USA) configured in current-clamp mode.

Histology

During recordings of at least 20 min, neurones were passively filled with biocytin. Vibratome sections (50 μm) containing biocytin-filled neurones were processed using standard histological procedures (Horikawa & Armstrong, 1988) and labelled cells were identified by light or fluorescence microscopy.

Data Analysis

Data was analysed offline using MATLAB 7.1 (The Mathworks, Inc., Natick, MA, USA) with Signal Processing 6.4 and Statistics 5.1 Toolboxes. Axon binary files were imported into MATLAB using a function written by John Bender (http://www.mathworks.de/matlabcentral/fileexchange/).

Assessment of responses to current steps

The membrane potential of all neurones at each time point was corrected by the estimated tip potential present at the time of recording. Cellular properties were estimated from membrane potential responses to a series of current pulses of 90 ms. The rheobase current was defined as the minimal current amplitude necessary to evoke an action potential. Input resistance was determined from the slope of a regression line fitted to four mean membrane potentials produced by a series of subthreshold current pulses (−0.2, 0, +0.2, +0.4 nA) during the Down state of the neurone. Whenever possible, voltage traces were averaged across several repetitions in order to minimize background noise. To minimize the influence of the slowly inactivating A-current, voltages were measured between 77 and 83 ms after start of the current injection. In CINs, to minimize the influence of I_H or spontaneous spikes, four minimal membrane potentials produced by a series of negative current pulses (−0.6, −0.4, −0.2, 0 nA) were used instead.

The membrane time constant (τ) was estimated from an exponential fit to the initial phase (22 ms) of membrane potential responses to injected current steps, $V(t) = A \times (1 - \exp(-t/\tau)) + V(0)$, where V denotes voltage depending on time t, and A the amplitude of the voltage response at $t = \infty$. The built-in MATLAB function 'fminsearch' was used to estimate the free parameters A and τ on four membrane potential responses (−0.4, −0.2, +0.2, +0.4 nA) and the membrane time constant was defined as the mean estimate of τ from subthreshold membrane potential responses. As a first approximation, the cell capacitance (C) was calculated from τ and input resistance (R), $C = \tau/R$.

Assessment of spontaneous activity

The distribution of the membrane potentials was assessed by all-amplitude histograms (0.3 mV resolution) of 30–90 s of continuous intracellular recording when the recording had stabilized shortly after impalement. Only data that did not include an apparent drift in the (Down state) membrane potential was included. On the all-amplitude histogram, the modal depolarised and hyperpolarised membrane potentials were determined as the maxima positive and negative to the transition threshold, respectively. A simple, but efficient threshold method was used to divide the membrane potential distribution into the Up and Down state according to the transition threshold (Schulz *et al.* 2009, 2010): the transition threshold was calculated as the arithmetic mean of the 80th and 20th percentiles of the membrane potentials. Up state transition parameters were measured on the smoothed membrane potential trace (3rd order Savitzky–Golay filter of 30 ms window width; Fig. 3*A*). The transition amplitude was defined as the difference between the minimal membrane potential preceding the Up state transition and the maximal membrane potential reached during 100 ms following the time of transition threshold crossing. The duration of the state transition was measured for the central 75% of the transition amplitude, in order to make this measurement less susceptible to noise around the extremes of the membrane potential states. The transition slope was calculated as 75% of the amplitude divided by the transition time. For the generation of mean Up state transitions and spike-triggered averages of the membrane potential, all action potentials were detected and removed from the membrane potential trace by setting

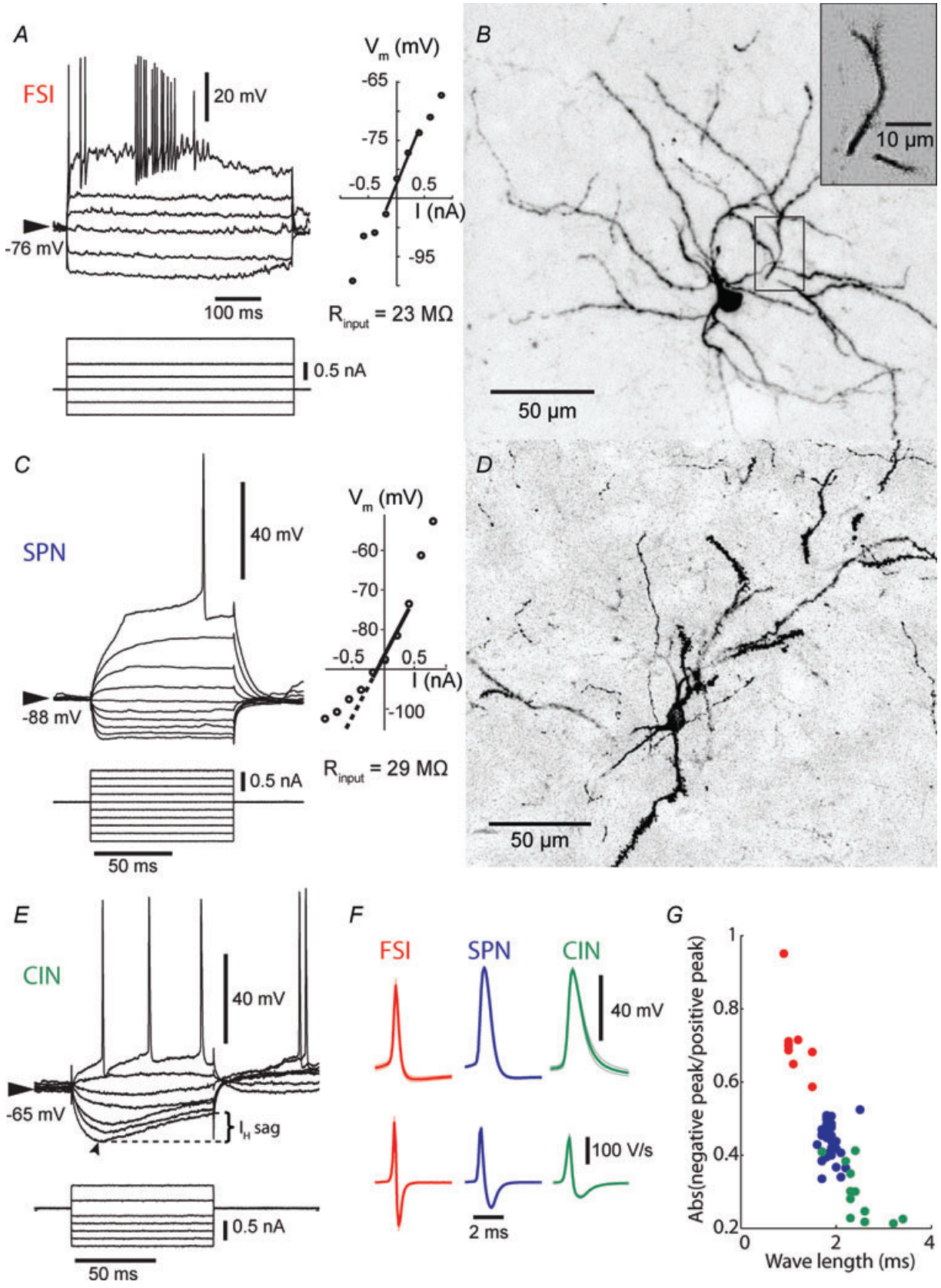

the membrane potential to the potential at the spike threshold (8 mV ms^{-1}) for the duration of the spike.

Spike statistics. The spike rate (Hz) was defined as the number of action potentials divided by the duration of the recording (s). For each pair of subsequent action potentials, the interspike interval (ISI) was calculated as the time difference between the maxima of the action potential. Histograms of the ISI distribution were calculated using the following bin boundaries in ms: 5, 10, 15, 25, 40, 65, 105, 170, 275, 445, 720, 1165, 1885, 3050, 4945, 8005. For plots, a logarithmic *x*-scale was chosen. This allowed the comparison of ISI distributions over a wide range of activity patterns.

Using the ISI, the coefficient of variation 2 (CV2) was calculated (Holt *et al.* 1996):

$$CV2_n = 2 \times \text{absolute}(ISI_n - ISI_{n-1})/(ISI_n + ISI_{n-1}),$$

where ISI_n is the inter-spike interval between spikes 2 and 3 and ISI_{n-1} is the inter-spike interval between spikes 1 and 2 in a series of three spikes. The CV2 ranges between 0 and 2 (with 0 indicating maximum regularity).

Spike waveform

Action potentials were isolated and aligned to the maximum. On each action potential, threshold, amplitude and half-width were measured. The spike threshold was defined as the time when the slope of the membrane potential exceeded 8 mV ms^{-1}. The amplitude was defined as the potential difference between the threshold and the maximum of the waveform. The half-width was defined as the width of the action potential at the point midway between threshold and maximum. The mean values for each neurone were saved for group analysis. As measurements of the action potential AHP were more susceptible to background noise, they were taken from the averaged spike waveform. The spike AHP amplitude was defined as the difference between the minimal potential and the mean firing threshold (8 mV ms^{-1}). The first derivative was calculated from the averaged waveform using a simple difference procedure: $dV(t)/dt = (V(t) - V(t_{n-1}))/(t_n - t_{n-1})$.

Time–frequency analyses

The power spectra of the membrane potential and the ECoG were estimated on data segments of 3 s using the fast Fourier transformation and averaged across all non-overlapping segments from 30 to 90 s of continuous recording. The time-resolved power spectrum of the membrane potential, aligned to Up state transition, was generated by calculating the power spectra for segments of 100 ms in steps of 50 ms. Time-resolved power spectra were averaged across all Up state transitions, and mean time-resolved power spectra from FSIs were normalized relative to those from control SPNs.

Correlation analyses

The exponential fit shown in Fig. 2*F* was performed in Microsoft Excel 2007. Crosscorrelograms were calculated between afferent population signals and the intracellular membrane potential using the MATLAB function 'xcov'.

Postsynaptic potential measurements

The maximal slope of single evoked postsynaptic potentials (PSPs) was taken from a linear fit with a sliding window of 1 ms width. The medians of the maximal slope and of the latency to maximal slope from stimulus onset were noted for each neurone. On the averaged PSP waveform, the amplitude and the rise time from 10% to 90% of the amplitude were measured.

Statistics

A non-parametric Wilcoxon's rank sum test was used for the assessment of differences in cellular properties between classes of neurones. Group data are presented as means ± standard deviation (SD) calculated across the

Figure 1. Electrophysiological and morphological characteristics of three classes of striatal neurones *in vivo*
A, membrane potential response of a FSI to linear current steps. Note the immediate and subsequently stuttering action potential discharge as well as the subthreshold membrane potential fluctuations in between. *B*, merged Z-projections from confocal image stacks of the same biocytin-filled neurone. The dendrites are smooth. *C*, membrane potential response of a SPN to linear current steps. Note the delayed action potential discharge. Inset shows the current–voltage relation; the input resistance was derived from the slope of the regression line. *D*, merged Z-projections from confocal image stacks of the same biocytin-filled neurone. The dendrites are densely studded with spines. *E*, electrophysiological characteristics of a CIN. Note the I_H-dependent sag response to hyperpolarising current injections. *F*, grandmeans of the spike waveform (top) and the first derivative (bottom) are shown for SPNs (blue; $n = 74$), FSIs (red; $n = 9$) and CINs (green; $n = 12$). Lighter colours indicate the SEM in all panels. *G*, plot of wavelength of the mean AP derivative *versus* ratio between positive and negative peak showing that the FSI spike waveforms were clearly different from other neurons.

Table 1. Cellular properties of three classes of striatal neurones *in vivo*

Response to current steps	FSIs ($n = 9$)	SPNs ($n = 90$; 74)	CINs ($n = 12$)
Input resistance (MΩ)	31.2 ± 14.0	34.0 ± 11.9	47.8 ± 11.4
Membrane time constant (ms)	3.1 ± 1.1	3.8 ± 1.5	7.8 ± 1.7
Cell capacitance (pF)	115.9 ± 51.1	122.6 ± 54.4	157.0 ± 48.7
Rheobase current (nA)	0.89 ± 0.32	0.93 ± 0.31	0.09 ± 0.17
Spike waveform			
Firing threshold (mV)	−52.4 ± 4.6	−52.9 ± 4.9	−54.5 ± 5.1
Amplitude (mV)	49.9 ± 9.4	63.1 ± 7.4	62.0 ± 5.9
Half-width (ms)	0.4 ± 0.1	0.8 ± 0.1	1.1 ± 0.3
AHP amplitude (mV)	10.6 ± 2.5	9.2 ± 2.9	8.1 ± 2.7
Membrane potential distribution			
Modal depolarised potential (mV)	−61.1 ± 3.5	−68.4 ± 6.1	−60.6 ± 4.0
Modal hyperpolarised potential (mV)	−78.2 ± 6.2	−86.2 ± 5.7	—
Difference (mV)	17.1 ± 5.1	17.8 ± 4.3	—
Spontaneous spiking properties			
Spike rate (Hz)	6.3 ± 6.7	1.4 ± 1.7	3.6 ± 2.6
Mean CV2	0.96 ± 0.23	1.25 ± 0.31	0.63 ± 0.25

Total numbers of neurones are indicated. For SPNs, the second number indicates spontaneously active neurones included in spiking properties and spike waveform measurements. Data are means ± SD across neurones.

mean values of individual neurones. For detailed analyses of paired data (Up state transitions, time-resolved power spectra and STA), Wilcoxon's signed rank test for paired samples was used. Error bars in graphs depict the error of the mean (SEM). The probability level for statistical significance was set at $P = 0.05$. For multiple tests on the time-resolved power spectra, the significance level was divided by the number of tests to correct for the increased probability of false positives.

Results

We used *in vivo* intracellular techniques to record spontaneous and stimulus-evoked membrane potential activity from striatal neurones. We obtained stable recordings from 111 neurones during urethane-induced ECoG slow-wave activity. All neurones were electrophysiologically identified and/or morphologically verified as belonging to one of three classes of striatal neurones. The vast majority of recordings was from SPNs ($n = 90$; Fig. 1*C*), while the interneurones consisted of 12 electrophysiologically identified CINs (Fig. 1*E*) and nine FSIs (Fig. 1*A*), the latter very rarely encountered and thus collected over a period of 11 years. Data from some neurones have been included in previous analyses on visual responsiveness and synaptic plasticity (Schulz *et al.* 2009, 2010). This paper instead focuses on the membrane potential dynamics of FSIs *in vivo* and compares this with other classes of striatal neurones recorded under similar conditions, even from the same animal where available.

Electrophysiological characteristics of FSIs

Fast-spiking interneurones were identified based on their spike waveform and firing properties (Kawaguchi, 1993; Plenz & Kitai, 1998; Koos & Tepper, 1999). Fast-spiking neurones fired at very high frequencies in response to suprathreshold current injections, in three of nine neurones without any delay (Fig. 1*A*, Table 1). Spontaneous action potentials were significantly smaller in amplitude ($P < 0.001$; Wilcoxon's rank sum test, $n_1 = 9$, $n_2 = 74$, ranksum = 137) and half-width ($P < 0.001$; ranksum = 45) than in SPNs (Table 1 and Fig. 1*F*), often without overshooting 0 mV ($n = 6$ of 9). The first derivative of the mean action potential of FSIs (Fig. 1*F*) exhibited properties similar to extracellular recordings from putative FSIs, consisting of a short, relatively symmetrical waveform (Berke *et al.* 2004; Mallet *et al.* 2005; Berke, 2008; Sharott *et al.* 2009). Plotting absolute wavelength of the action potential derivative versus ratio between positive and negative peak revealed a clear distinction between FSIs and other striatal neurones (Fig. 1*G*). Morphological assessment of the four FSIs that could be recovered after intracellular biocytin-filling confirmed that the medium-sized neurones had mostly smooth dendrites (Fig. 1*B*) similar to previous descriptions of GABA/parvalbumin-positive

interneurones (Kawaguchi, 1993; Plenz & Kitai, 1998; Koos & Tepper, 1999). Therefore, we concluded that our FSIs corresponded to FSIs recorded in previous *in vitro* and *in vivo* extracellular recording studies. We were therefore able for the first time to investigate the membrane potential dynamics that control spiking in these neurones *in vivo*.

We assessed the passive and active electrophysiological membrane properties by injecting short current steps of increasing amplitude through the pipette (Fig. 1). The input resistance and membrane time constant were similar to those of SPNs (Table 1). Furthermore, there was no difference in the rheobase between FSI and SPNs, indicating that FSIs required comparable amounts of somatic inward current to reach action potential threshold. In contrast, the CINs were clearly different in all cellular properties from both SPNs and FSIs (Table 1).

Up and Down state-fluctuations in striatal neurones

Spiny projection neurones exhibited prominent membrane potential fluctuations between a hyperpolarised Down state and depolarised Up state that was associated with occasional spike discharge (Fig. 2*B*). This resulted in a bimodal membrane potential distribution and irregular spike statistics (Fig. 2). The Up and Down state membrane potential fluctuations in SPNs during anaesthesia are known to be tightly correlated to activity in somatosensory and motor cortices (Wilson *et al.* 1983; Mahon *et al.* 2001; Tseng *et al.* 2001; Kasanetz *et al.* 2006). In most experiments in this study, when the ECoG was recorded from the primary visual area (Schulz *et al.* 2009), the SPN membrane potential fluctuations were only weakly correlated to the ECoG in this area.

Previous reports on extracellular recordings from putative FSIs under urethane anaesthesia suggested that their firing pattern is modulated by cortical afferents in a similar fashion to SPNs (Mallet *et al.* 2005). In our sample of *in vivo* intracellular recordings, all FSIs exhibited Up and Down state-like membrane potential fluctuations (Fig. 2*A*). Similar to other striatal neurones, the membrane potential fluctuations were clearly correlated to the ECoG (Fig. 2*A*; for an example with the ECoG from contralateral sensorimotor cortex see the Supplemental Material, Fig. S1). Although the amplitude of state transitions varied between neurones, the pattern was very similar to those in SPNs in most cases, and distinctly different from membrane potential fluctuations in CINs (Fig. 2*C*; a detailed analysis of the correlation with the ECoG can be found in Schulz *et al.* 2011). Consistently, the all-amplitude histograms of the membrane potential exhibited a two-modal distribution. The difference between modal depolarised and hyperpolarised membrane potential was 17.1 ± 5.1 mV, almost identical to those in SPNs (Table 1). In contrast, both the depolarised ($P < 0.001$; Wilcoxon's rank sum test, $n_1 = 9$, $n_2 = 90$, ranksum = 736.5) and the hyperpolarised membrane potential were significantly more depolarised than in SPNs ($P = 0.002$; ranksum = 710.5; Table 1). As there was no difference in the action potential threshold between FSIs and SPNs (-52.4 ± 4.6 mV and -52.9 ± 4.9 mV, respectively), this indicated that the modal depolarised membrane potential of -61.1 ± 3.5 mV in FSIs tended to be much closer to the action potential threshold than in SPNs (-68.4 ± 6.1 mV). Consistently, spontaneous spike rates were significantly higher in FSIs than in SPNs ($P = 0.004$; Wilcoxon's rank sum test, $n_1 = 9$, $n_2 = 90$, ranksum = 579). The spontaneous spike rates of FSIs ranged from 0.4 to 21.2 Hz. Non-linear correlation analyses confirmed the prediction that the difference between modal Up state membrane potential and spike threshold was one important factor determining the average spike frequency in both classes of neurones (Fig. 2*F*).

Spike statistics of striatal neurones

When FSIs spiked during the Up state, they tended to fire at higher frequencies than SPNs (Fig. 3*G* top). This was also evident in the mean ISI distribution, with a high proportion of small ISIs of <30 ms (Fig. 2*D*, Table 2). The ISI distribution was bimodal, similar to SPNs; however, there was an obvious leftward shift of the peak of short ISIs. In contrast to both SPNs and FSIs, the ISI distribution in CINs showed a prominent peak at intermediate intervals of 100–300 ms (Fig. 2*D*, Table 2), corresponding to the mean spike rate of 6.3 ± 6.7 Hz (Table 1). The distribution of CV2 values calculated on adjacent ISIs showed a particularly high percentage of small values (Fig. 2*E*). Thus, the mean CV2 of ISIs in CINs was significantly smaller than in SPNs ($P < 0.001$; Wilcoxon's rank sum test, $n_1 = 12$, $n_2 = 74$, ranksum = 107). In FSIs, the mean CV2 was also smaller than in SPNs ($P = 0.008$; Wilcoxon's rank sum test, $n_1 = 9$, $n_2 = 74$, ranksum = 195; Table 1). The CV2 distribution of FSIs lay in between SPNs and CINs (Fig. 3*D*), due to the longer spike trains of relatively regular ISIs during the Up state and the relatively small contribution of long ISI between Up states to the population of ISI values. In summary, the spike statistics revealed clear differences between the three classes of striatal neurones on the population level. SPNs fired at very irregular intervals, while both interneurone classes exhibited more regular spiking in distinct frequency bands

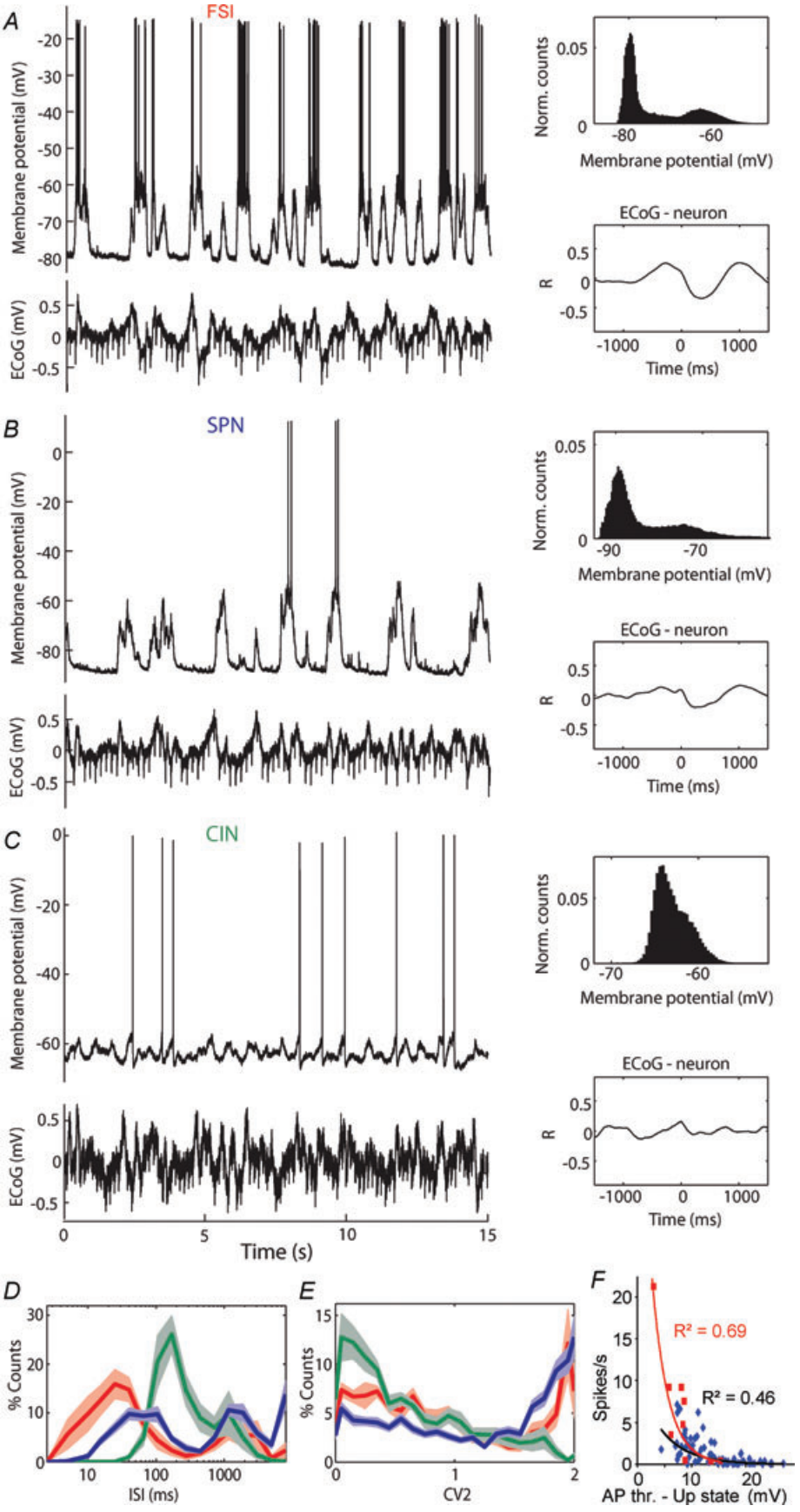

(Table 2). Yet, within both classes of interneurones there were examples that superficially resembled SPNs because of a very low spike rate (data not shown), suggesting that the spike pattern alone may not be sufficient to identify individual neurones (e.g. extracellular recorded single unit activity).

Comparison of Up state transitions in FSIs and SPNs

Having established the overall similarity in Down state–Up state pattern between FSIs and SPNs *in vivo*, we next compared the fine temporal structure of Up state transitions between them. Using a simple threshold procedure (Fig. 3*A*; see Methods for details), we detected all spontaneous Up state and aligned them to the state transition (see examples in Fig. 3*B* and *C*). To minimize experimental differences between SPN and FSI recordings, only recordings from SPNs from the same animal ($n = 4$), if available, or a subsequent experiment by the same experimenter ($n = 5$) were included in the analysis of Up transitions (Fig. 3) and evoked postsynaptic potentials (PSPs; Fig. 4*B*). This showed that median amplitude (FSI: 12.8 ± 3.8 mV; SPN: 14.8 ± 3.7 mV), slope (FSI: 0.13 ± 0.07 mV ms^{-1}; SPN: 0.17 ± 0.05 mV ms^{-1}) and duration (FSI: 107.0 ± 37.6 ms; SPN: 88.9 ± 25.2 ms) of the Up transition were no different between classes of neurones (all: $P > 0.1$; Wilcoxon's signed rank test, $n = 9$; Fig. 3*G* middle). However, when we investigated the power spectra of the spontaneous recording, we found that FSIs tended to exhibit lower power in frequencies below 20 Hz than SPNs, but that frequencies above 40 Hz were clearly enhanced (Fig. 3*D*). Analysis of the time-resolved power spectra of the membrane potential relative to the Up transition showed that the power of high frequencies in FSIs was specifically enhanced during the Up state (Fig. 3*E*). In SPNs, the power of most frequencies was strongly enhanced during the short transition to rather than during the Up state (Fig. 3*F*). Comparing the time-resolved power spectra between neurone classes, we found that the Up state membrane potential of FSIs had a much higher content of high-frequency components (55–95 and 105–145 Hz; Fig. 3*G* bottom). *In vitro*, striatal FSIs exhibit subthreshold membrane potential oscillations in the gamma frequency range (~40 Hz) in response to positive near-suprathreshold current injections that depend on activation of Na^+ channels (Bracci *et al.* 2003). In our sample of *in vivo* recordings, similar oscillations were obvious in two-thirds of FSIs (see example in Fig. 1*A*), suggesting that intrinsic ionic mechanisms may have contributed to enhanced gamma-frequency oscillations in response to natural synaptic inputs during the Up state.

Influence of membrane potential fluctuations on spike initiation

Given that some FSIs tended to spike at frequencies similar to the enhanced fast membrane fluctuations, we asked ourselves whether spiking in FSIs was mainly driven by small-amplitude high-frequency membrane potential fluctuations, and whether this differed from SPNs. In order to see which events led to spike discharge, we next investigated spike-triggered averages of the membrane potential. Membrane potential trajectories showed a slow depolarisation of almost 10 mV preceding a spike in SPNs (Fig. 3*H* top). In contrast, spikes in FSIs were generally not preceded by such a large-amplitude ramp depolarisation. Indeed, the slope of the membrane potential was significantly steeper in SPNs than in FSIs (SPN: 0.42 ± 0.09 mV ms^{-1}; FSI: 0.27 ± 0.12 mV ms^{-1}; $P = 0.008$; Wilcoxon's signed rank test, $n = 9$, signed rank $= 1$) when measured over the 10 ms prior to action potential threshold (8 mV ms^{-1}). When a sliding window of 1 ms was used for the calculation of the slope (Fig. 3*H* middle), it became evident that the slope tended to divert from zero only 5 ms before the AP in FSIs, whereas the slope was much more variable before this time than in SPNs (Fig. 3*H* bottom). This indicated that the slope of the membrane potential in FSIs exhibited larger fluctuations than in SPNs, and that these fluctuations affected the spike discharge on a relatively short time scale. This was consistent with the idea that small high-frequency membrane potential fluctuations drove spiking in FSIs, whereas spiking in SPNs was driven by slower and larger depolarisations.

Figure 2. Spontaneous activity patterns of three classes of striatal neurones during urethane-induced slow-wave ECoG activity *in vivo*
A–C, segments of intracellular and simultaneous ECoG recordings (left), membrane potential distribution over the whole 90 s recording (top right), and cross-correlograms between intracellular and extracellular ECoG activity (bottom right) for a representative FSI (*A*), SPN (*B*) and CIN (*C*). Cardiovascular artefacts are evident in the ECoG traces. *D*, mean distribution of interspike intervals (ISI) for all three neurone classes. Note the bimodal distribution in SPNs (blue; $n = 74$) and FSIs (red; $n = 9$) in contrast to the unimodal distribution at intermediate ISIs in CINs (green; $n = 12$). *E*, mean distribution of CV2 values. Note the high proportion of small CV2 values in CINs and the high proportion of high CV2 values in SPNs. *F*, dependence of spike rate on the membrane potential depolarisation during the Up state in SPNs and FSIs.

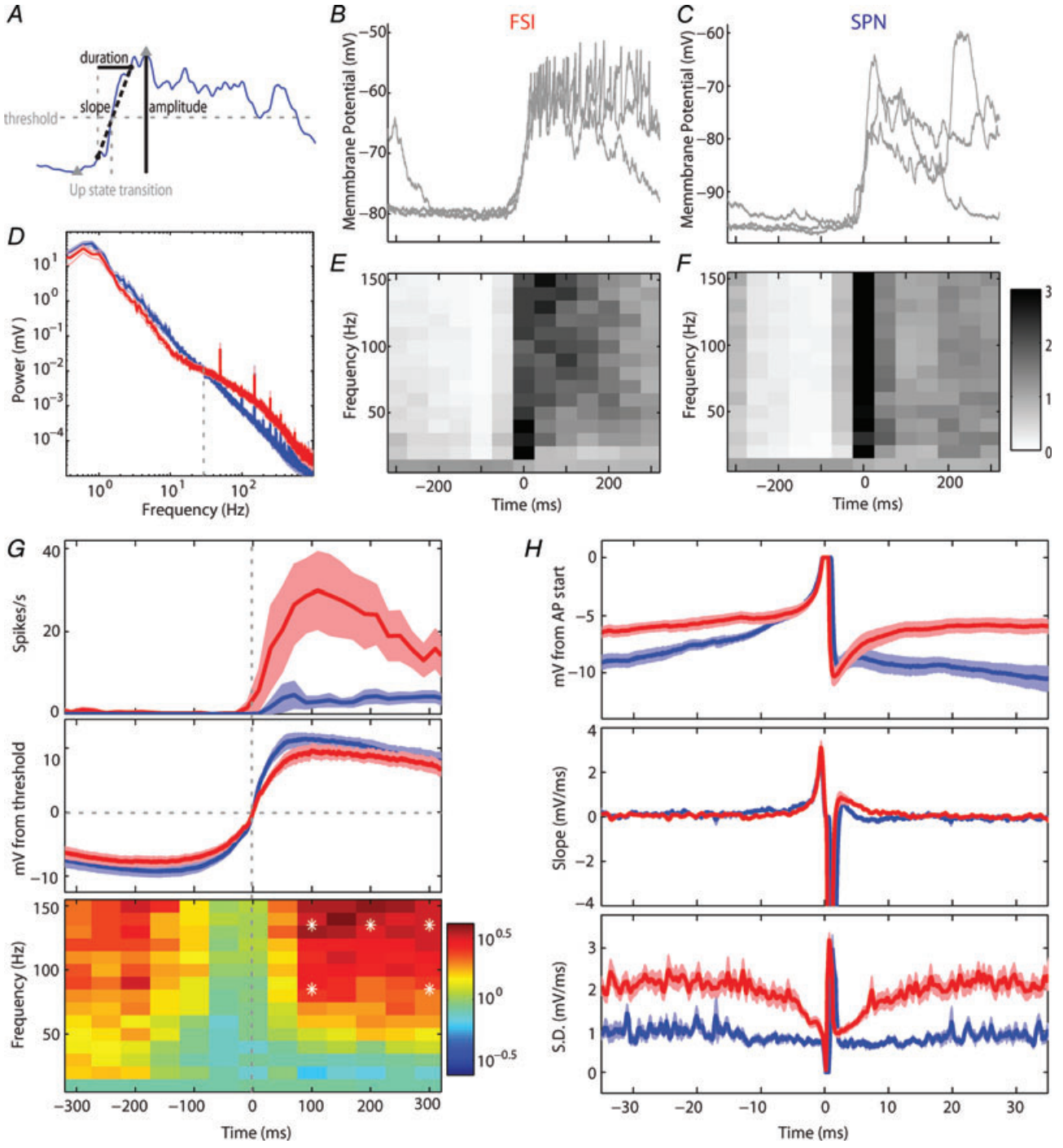

Figure 3. A comparison of slow and fast membrane potential fluctuations in SPNs and FSIs recorded during ECoG slow-wave activity

A, measurements of parameters of Up state transitions on the smoothed membrane potential recording (3rd order Savitzky–Golay, 30 ms window). For definition of parameters see Methods. *B* and *C*, three Up states aligned to the transition threshold in the same FSI (*B*) and SPN (*C*) as in Fig. 2. Action potentials have been removed from traces for the calculation of the membrane potential power spectra. *D*, mean log-scale power spectra of the membrane potential over the whole recording segment for FSIs (red) and SPNs (blue; both: $n = 9$). Note the non-linear decay in FSIs in this chart and the cross-over of the spectra from FSIs and SPNs at ~30 Hz (dashed line). *E* and *F*, the mean normalized time-resolved power spectrum relative to the Up state transition are shown for the same neurons as in *B* and *C*. The grey coding is according to a linear scale (right), where 1 represents the average power for the respective frequency band. *G*, mean Up state transition aligned to the transition threshold in FSIs (red) and SPNs (blue; both: $n = 9$). Lighter shades indicate SEM. Upper panel, FSIs tended to larger spike rates during the Up

Table 2. Percentage of inter-spike intervals according to classical ECoG frequency bands

Frequency band ISIs	Slow and delta <4 Hz >250 ms	Theta–alpha, 4–12.5 Hz 250–80 ms	Beta, 12.5–33 Hz 80–30 ms	Gamma, >33 Hz <30 ms
SPNs ($n = 68$)	53.3 ± 28.2%	16.2 ± 14.2%	19.3 ± 16.4%	11.1 ± 15.0%
pBIC ($n = 8$)	49.0 ± 26.9%	25.8 ± 17.3%	20.8 ± 19.6%	4.3 ± 6.4%
CINs ($n = 12$)	43.2 ± 31.8%	52.1 ± 28.4%	4.7 ± 5.7%	0.0 ± 0.1%
pBIC ($n = 6$)	28.7 ± 27.5%	63.6 ± 21.1%	7.8 ± 7.6%	0%
FSIs ($n = 9$)	29.9 ± 30.0%	4.9 ± 3.4%	21.6 ± 12.6%	43.6 ± 32.8%
pBIC ($n = 1$)	3.0%	1.3%	11.1%	84.4%

Data are means ± SD across spontaneously spiking neurones during slow-wave and desynchronized ECoG activity post BIC ejection into the superior colliculus (pBIC).

Cortical evoked postsynaptic potentials. Next, we investigated if there were any differences in cortical synaptic inputs between neurone classes. In four of the nine FSI–SPN pairs, PSPs were evoked by stimulating the contralateral motor cortex during the hyperpolarised Down state in both neurones. The amplitude of the mean PSP (SPNs: 6.8–13.7 mV; FSIs: 7.7–16.2 mV) and median latencies to maximal slopes in individual traces (SPNs: 5.8–10.5 ms; FSIs: 6.7–10.1 ms) were similar. In contrast, the rise time of the mean PSP was consistently shorter in FSIs (SPNs: 5.6–11.1 ms; FSIs: 4.2–4.9 ms), and the median maximal slope was consistently larger in FSIs in all four cases (SPNs: 2.0–3.9 mV ms^{-1}; FSIs: 3.2–5.9 mV ms^{-1}). The faster dynamics were also evident in the grand mean of the PSP (Fig. 4*B*).

A different set of neurones was repetitively exposed to cortical high-frequency stimulation (HFS; 100 Hz over 500 ms). Cortical HFS was accompanied by a suprathreshold current injection to ensure postsynaptic spike discharge, as commonly used in studies on striatal synaptic plasticity (Calabresi *et al.* 1992; Reynolds & Wickens, 2000). When we investigated the spike pattern evoked by this protocol, we found that most SPNs spiked only transiently during the stimulation (Fig. 4*A*). Spiking in SPNs ($n = 6$) was also poorly entrained to evoked synaptic inputs, as evident in the broadly distributed ISI distribution that lacked a peak at 10 ms (i.e. 100 Hz; Fig. 4*C*). In another set of experiments, we therefore used stimulation at intermediate frequencies (20 Hz) and found that this strongly entrained spike output in SPNs (Fig. 4*A*, lower panel), as indicated by the prominent peak at 50 ms (i.e. 20 Hz) in the ISI distribution (Fig. 4*C*, bottom). Neurones were also more likely to spike throughout the stimulation protocol ($n = 5$). This indicated that the spike output of SPNs failed to follow input sequences specifically when these were presented at high frequency. In contrast, the recording from one FSI was suggestive for the idea that this interneurone class more readily follows high-frequency inputs (Fig. 4*A*, top).

Influence of the brain state on membrane potential fluctuations and spike output

Lastly, we investigated the effect of pharmacologically induced ECoG desynchronisation, i.e. disruption of large amplitude slow-wave ECoG activity, on the membrane potential of striatal neurones. As previously shown (Schulz *et al.* 2009), bicuculline (BIC) ejection into the superior colliculus induced a strong decrease in the ECoG power at low frequencies (Fig. 5*A*). Under these conditions, slow oscillatory activity was diminished in all striatal neurone classes (Fig. 5*B* to *D*), i.e. the Up and Down state activity pattern was disrupted in SPNs and FSIs. Yet, the overall structure of the population ISI distribution remained almost unchanged (Table 2). In four of 21 SPNs investigated, the spike rate was increased from a very low rate (0.01–0.3 Hz) to 3.2–4 Hz immediately after BIC ejection. At the same time, the high-frequency content of membrane potential fluctuations in SPNs was mildly increased by 43 ± 55% at 55–95 Hz and 59 ± 87% at 105–145 Hz (both: $P < 0.01$; Wilcoxon's signed rank test, $n = 13$; Fig. 5*C*), respectively. For CINs, the same pharmacological activation of the SC resulted in membrane potential depolarisation and significantly increased spike rates (Schulz *et al.* 2011). Nonetheless, the structure of the population ISI distribution changed

state, while membrane potential trajectories during the transition were very similar between FSIs and SPNs (central panel). Lower panel, the mean time-resolved power spectrum from FSIs normalized relative to SPNs. The colour coding according to log-scale is shown on the right. FSIs exhibited larger fast membrane potential oscillations than SPNs specifically during the Up state (indicated by the white stars, $P < 0.01$). *H*, spike-triggered average of the membrane potential (top), the slope (middle), and the standard deviation of the slope (bottom) show that fast membrane potential fluctuations precede spike discharges in FSIs.

little (Table 2). There was also no significant effect on the high-frequency content of the subthreshold membrane potential for the population of CINs post BIC (55–95 Hz and 105–145 Hz, both $P > 0.05$; Wilcoxon's signed rank test, $n = 8$; Fig. 5*D*). In striking contrast to both SPNs and CINs, the membrane potential of the one FSI tested exhibited strong increases in high-frequency fluctuations of 779% at 55–95 Hz and 959% at 105–145 Hz (Fig. 5*B*). At the same time, the firing rate was dramatically increased from 2.5 to 30.0 Hz, with the vast majority of ISIs (84.4%) in the gamma range (Table 2).

In summary, FSIs tended to exhibit much more pronounced fast membrane potential fluctuations than either CINs or SPNs under all experimental conditions *in vivo*. Thus, fast membrane potential dynamics controlled the spike output in FSIs, while much slower membrane potential dynamics promoted spiking in SPNs and CINs.

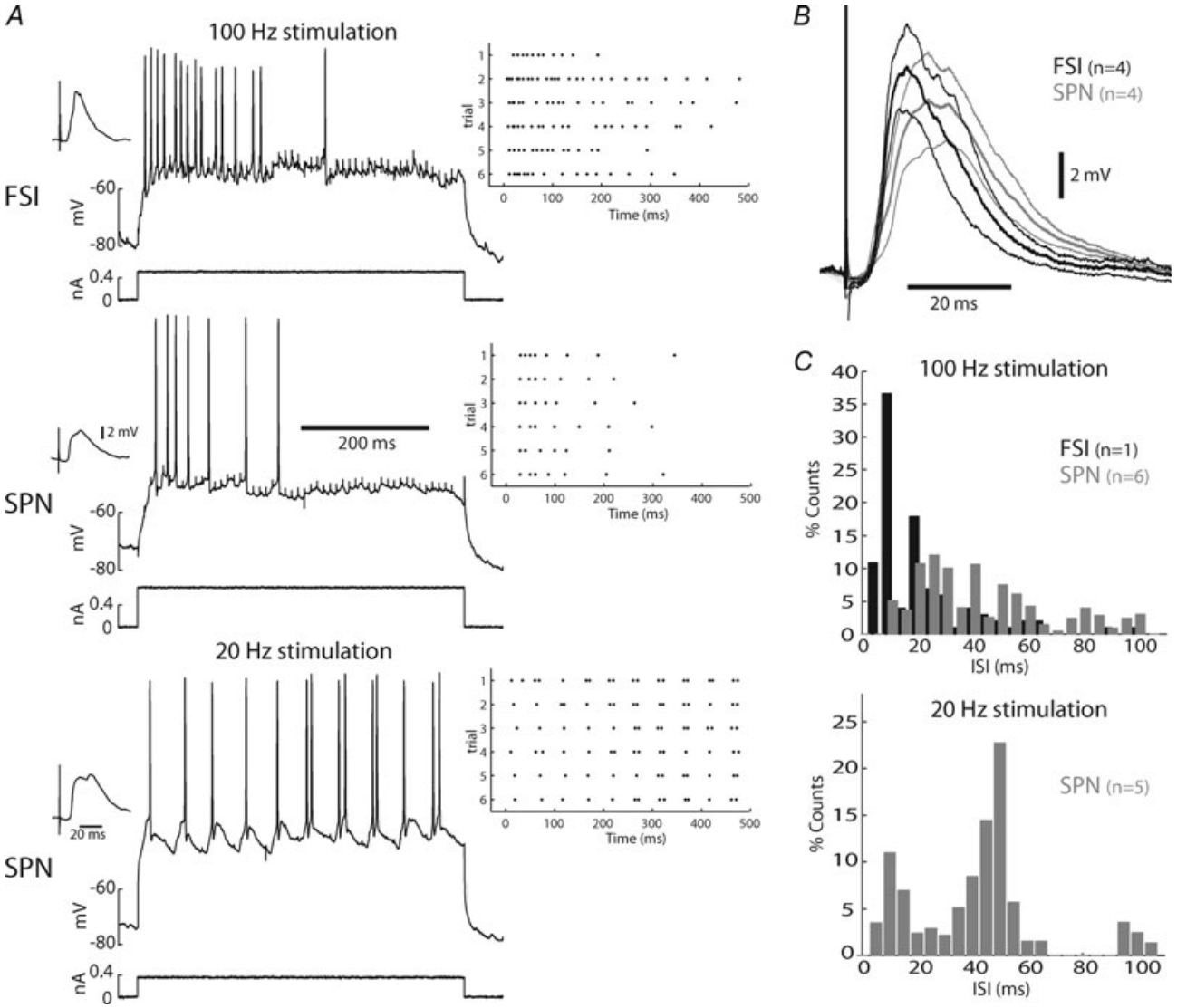

Figure 4. Entrainment of striatal neurones by repetitive synaptic stimulation
A, example traces of responses to stimulation of the contralateral motor cortex at 100 Hz or 20 Hz in a FSI and two SPNs. Left inset shows the mean PSP evoked by a single stimulation during the Down state. Central trace shows a response to repetitive stimulation and concomitant intracellular current injection. Right inset shows the spike response in six repetitions. The scale is the same for all three examples. For clarity, stimulus artefacts have been truncated. *B*, grand mean of the evoked PSP in four FSIs and SPNs recorded in the same or a subsequent experiment. Lighter traces indicate the SEM. *C*, histograms of ISIs evoked by repetitive synaptic stimulation. Note the absence of a peak at 10 ms, when SPNs were stimulated at 100 Hz, and the presence of a peak at 50 ms, when stimulated at 20 Hz.

Discussion

The present study is to the best of our knowledge the first comprehensive study of the *in vivo* membrane potential dynamics in FSIs of the striatum. Our main results showed that slow membrane potential fluctuations of FSIs were very similar to those observed in SPNs, including the occurrence of Up and Down states; however, there were prominent fast membrane potential fluctuations specifically at times of strong synaptic activity that controlled spike output and accounted for a high percentage of small ISIs in FSIs. This study demonstrates for the first time how fast membrane potential fluctuations promote regular spiking at gamma frequencies in FSIs of the striatum *in vivo*. In the following, we will first address the limitations of this study and then discuss the involved mechanisms and functional implications.

Limitations

One important limitation of the present study was the small sample size of FSI recordings due to the rarity of these neurones and the difficulty in maintaining stable impalement using intracellular recording methods. Furthermore, FSIs comprise a heterogeneous group of interneurones (Kawaguchi, 1993) and other extremely rarely encountered interneurones, like calretinin and tyrosine hydroxylase-positive interneurones, may in principal have a similar electrophysiological phenotype (Tepper *et al.* 2010). In particular, the results obtained by cortical stimulation of synaptic inputs and disinhibition of the superior colliculus are at risk of representing accidental variations. However, comparing these results with the published literature we find that our observations are in good agreement with the general picture of FSI physiology. Thus, FSIs in the striatum and hippocampus have been reported to exhibit particularly fast dynamics in synaptic and dendritic transmission (Fino *et al.* 2008; Norenberg *et al.* 2010). Despite a restricted data set, we found indications that these faster PSP dynamics may also be a prominent feature of cortico-striatal synaptic transmission *in vivo*. The HFS experiments suggested that these protocols may be better suited to activate FSIs than SPNs. In agreement, a recent study (Gruber *et al.* 2009) on SPNs in the ventral striatum found that a similar cortical stimulation protocol (10 pulses at 50 Hz plus intracellular current step) rarely induced spiking in SPNs, but readily activated two FSIs. We found furthermore that induction of a cortical activated state mildly affected SPN output, whereas the output of one FSI was dramatically increased. Again, observations of increased spike activity of FSIs during activated ECoG states have been made with extracellular recordings (Mallet *et al.* 2005). Therefore, these results are unlikely to be accidental outcomes. Instead, our observations of the underlying membrane potential dynamics may provide novel insights into the mechanisms that control spike output in FSIs *in vivo*.

Mechanisms underlying enhanced fast oscillations

Fast-spiking interneurones exhibited prominent fast membrane potential fluctuations when the neurone was depolarised to near-threshold level. These oscillations in the gamma range were also evident as a hump in the double-logarithmic power spectra of the membrane potential at frequencies >30 Hz. The deviation of the FSI power spectra from the power-law frequency scaling, i.e. linear decay of the double-logarithmic power spectra, was in striking contrast to both SPNs and CINs. What factors could explain this observation?

Dynamics of synaptic inputs. Theoretical studies proposed that the frequency scaling of the membrane potential power spectra reflects the kinetics of individual synaptic currents/potentials (Destexhe & Rudolph, 2004). Since there is evidence that excitatory synaptic potentials in FSIs have faster dynamics than in SPNs, this factor probably contributed to a shallower decay slope of the power spectra in FSIs. At the same time, it is not likely to be the cause of the deviation from the power-law scaling.

Input correlations. A recent experimental study demonstrated that input statistics also affect the scaling of membrane potential power spectrum (El Boustani *et al.* 2009). Fast-spiking interneurones are more likely to receive convergent input from distinct cortical areas than SPNs, but receive more inputs from fewer cortical neurones (Ramanathan *et al.* 2002), suggesting that inputs exhibit a high degree of correlation. This may have added to the relatively noisy membrane potential.

Intrinsic mechanisms of resonance. Fast-spiking interneurones are known to autonomously generate membrane potential fluctuations of 30–40 Hz when depolarised near action potential threshold *in vitro* (Bracci *et al.* 2003). In the hippocampus, FSIs have been shown to act as resonators to sinusoidal current injections of gamma-range frequencies (Pike *et al.* 2000). Both phenomena are tetrodotoxin sensitive and therefore depend on the availability of Na^+ conductances. In fact, theoretical considerations suggest that both observations are two sides of the same mechanism (Hutcheon & Yarom, 2000): in addition to the natural low-pass filtering of neuronal membranes, voltage-sensitive rectifying conductances with slow activation kinetics can act as a high-pass filter; together, these filters can act as band-pass filters, thus, creating a resonator at a specific frequency range. Now, other voltage-sensitive conductances with relatively depolarised reversal potential, like the persistent

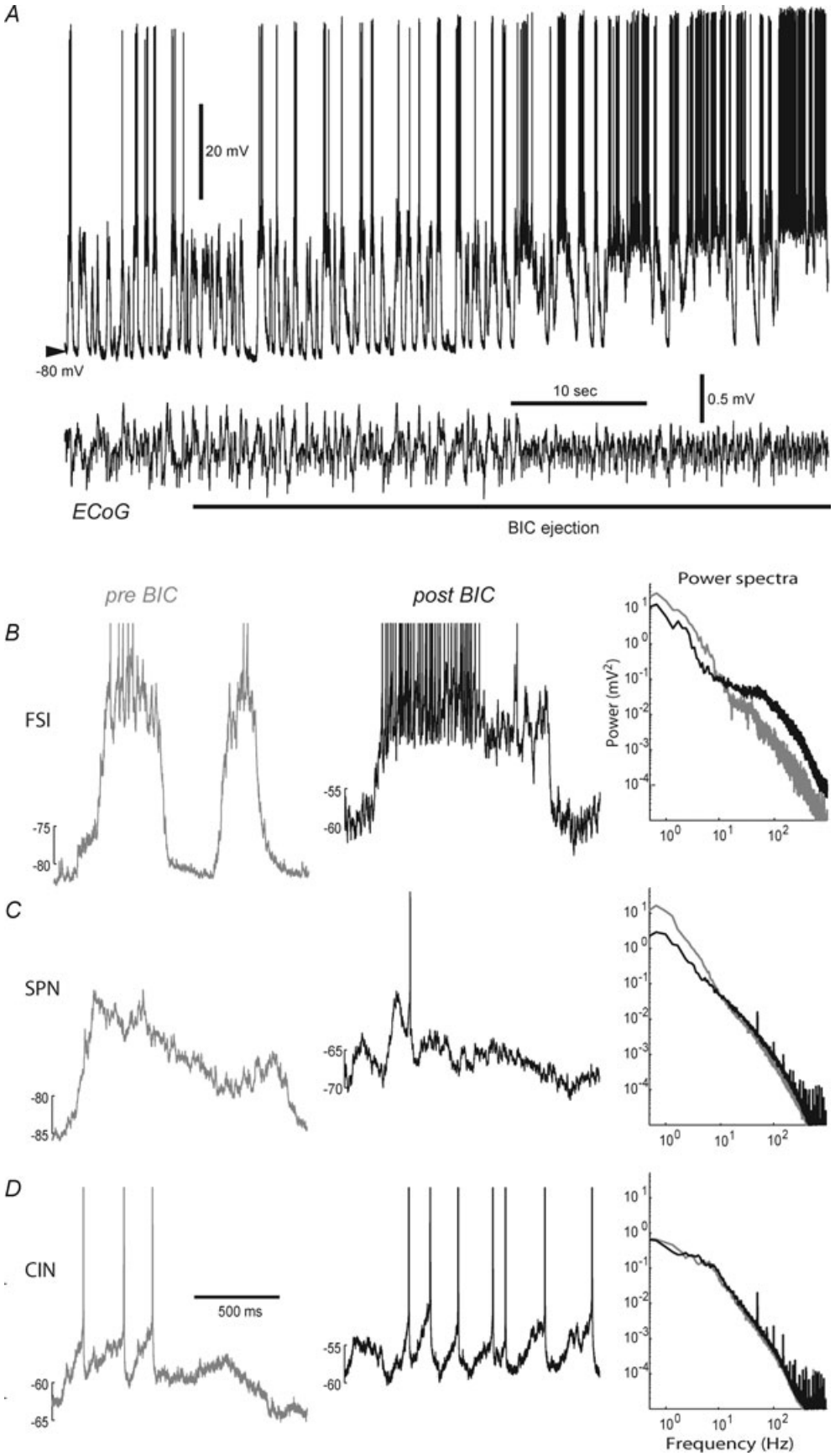

Na^+ conductance, can amplify signals at the resonance frequency. A recent modelling study confirms that the generation of subthreshold membrane oscillations at a depolarised membrane potential in FSIs may be a direct result of the interplay between Na^+ and K^+ conductances (Golomb *et al.* 2007). Thus, FSIs could act as amplifying resonators of high-frequency signals. The present study suggests that this mechanism is effectively engaged by synaptic inputs *in vivo*.

Functional implications

Cellular mechanisms of high-frequency amplification could promote gamma network oscillations that are suggested to underlie attention. Due to their cellular properties and connectivity, cortical and hippocampal FSIs have strongly been implicated in the generation of gamma oscillations (Bartos *et al.* 2007; Wang, 2010). Although it is not clear whether FSIs in the striatum generate gamma oscillations *de novo* because of the absence of recurrent excitatory inputs (Wang, 2010), the amplification of high-frequency inputs by FSIs may be a mechanism to entrain the local striatal network to gamma oscillations during action selection and reward-related learning (Tort *et al.* 2008; Berke, 2009). A recent study in behaving rats showed that FSIs tended to discharge at high frequency specifically when the animal had to choose between alternative actions (Gage *et al.* 2010). Furthermore, striatal FSIs are entrained to cortical gamma-oscillations during halothane-anaesthesia (Sharott *et al.* 2009) and to local gamma oscillations and high-voltage spindles in awake rats (Berke *et al.* 2004; Berke, 2009). The HFS results from this and another recent study (Gruber *et al.* 2009) further support the idea that inputs in the gamma frequency range are better suited to entrain FSIs than SPNs. In contrast, inputs at a beta frequency (20 Hz) were suited to entrain SPNs. Therefore, it appears that SPNs integrate synaptic inputs over slower time scales than FSIs and shape activity in the basal ganglia accordingly (Berke, 2009; Gage *et al.* 2010). It also suggests that traditionally used HFS protocols for the induction of synaptic plasticity are not suited to activate the targeted SPNs, while they readily activate coincident inhibitory inputs from neighbouring FSIs. The responsiveness of FSIs to high-frequency input sequences may be selectively increased during periods of cortical desynchronisation (Mallet *et al.* 2005), such as those after BIC ejection in the current study. Apart from an altered level and pattern of glutamatergic inputs from cortex and thalamus, a fundamentally altered neuromodulatory milieu, including changes in ambient dopamine and serotonin levels (Dringenberg *et al.* 2003; Dommett *et al.* 2005), may contribute to increased excitability of FSIs during these periods (Bracci *et al.* 2002; Blomeley & Bracci, 2009). One conclusion from these observations could be that striatal networks may be dominated by inhibition either from FSIs or from SPNs, depending on the dominant cortical input frequencies. However, even under conditions of increased FSI-mediated inhibition, some SPNs will continue to provide spike output that may be even enhanced as evident in the present study during the desynchronized ECoG activity post BIC. Thus, FSI-mediated feed-forward inhibition could act as a temporal gate for transient synaptic inputs as well as an amplitude gate for sustained activity (Mallet *et al.* 2005; Gruber *et al.* 2009; Kremkow *et al.* 2010). Gap junctions between neighbouring FSIs may serve this function by increasing the sensitivity to shared synchronous inputs while not increasing synchronous spiking between FSIs *per se*, as suggested by a recent computational study (Hjorth *et al.* 2009). An open question is whether this gating is pathway specific (Gittis *et al.* 2010; Planert *et al.* 2010). At the same time, FSIs may regulate the spike output of active SPNs in a rhythmic fashion. The increase in power of gamma-range membrane potential oscillations in SPNs post BIC could be indicative of such a mechanism. Therefore, FSIs may be responsible for several effects observed in recent studies in the ventral striatum of awake rats and cats (Berke, 2009; Popescu *et al.* 2009): (1) up to a quarter of recorded units were entrained to local gamma-frequency local field potential oscillations; (2) long range synchronisation of gamma activity with afferent networks in prefrontal cortex and amygdala could be demonstrated; and (3) there was a significantly higher cross-correlation between units in striatum

Figure 5. Effects of pharmacologically induced ECoG activation on fast membrane potential fluctuations in three classes of striatal neurones
A, immediate effects of the BIC ejection onto the membrane potential and spiking of a FSI. The time of the ejection is indicated. Note the dramatically increased spike frequency as soon as the ECoG activity loses the dominant slow wave oscillations. For clarity, cardiovascular artefacts have been removed from the ECoG trace by low-pass filtering (cutoff at 45 Hz). *B*, 1.5 s long membrane potential traces before and after BIC for the same neuron. Right inset shows the effect on the mean power spectrum of the membrane potential. Note the dramatically increased noise in the membrane potential post BIC (black). *C*, membrane potential traces before and after BIC for a SPN. Note the mild increase in high frequencies (>50 Hz) after the BIC ejection for the group of SPNs ($n = 13$). *D*, no change could be detected in the mean power spectra of CINs ($n = 8$). The scale is the same for all traces and neurons. The membrane potential offset is different for traces post BIC. Action potentials have been truncated.

and amygdala during periods of long-range gamma synchronisation.

Interestingly, CINs did not show any increase in the gamma frequency power post BIC. An anatomical investigation suggested that CINs do not receive direct inputs from parvalbumin-positive interneurones, while CINs synapse onto parvalbumin-positive neurones (Chang & Kita, 1992). Thus, CINs are likely to regulate spiking in FSIs, but not vice versa. In contrast to FSIs, CINs generate slow regular pacemaker spiking that is often, but not always correlated with cortical slow-wave activity, and is significantly affected by thalamic inputs in response to salient sensory events (Schulz *et al.* 2011). Therefore, CINs may serve the gating of information flow in response to salient sensory signals (Ding *et al.* 2010), while FSIs may mediate top-down control of SPNs by cortical networks during high gamma activity. In addition to more experimental work, it will be informative to include explicitly resonance properties of FSIs in modelling studies to address this hypothesis in the future.

References

Bartos M, Vida I & Jonas P (2007). Synaptic mechanisms of synchronized gamma oscillations in inhibitory interneuron networks. *Nat Rev Neurosci* **8**, 45–56.

Berke JD (2008). Uncoordinated firing rate changes of striatal fast-spiking interneurons during behavioral task performance. *J Neurosci* **28**, 10075–10080.

Berke JD (2009). Fast oscillations in cortical-striatal networks switch frequency following rewarding events and stimulant drugs. *Eur J Neurosci* **30**, 848–859.

Berke JD, Okatan M, Skurski J & Eichenbaum HB (2004). Oscillatory entrainment of striatal neurons in freely moving rats. *Neuron* **43**, 883–896.

Blomeley CP & Bracci E (2009). Serotonin excites fast-spiking interneurons in the striatum. *Eur J Neurosci* **29**, 1604–1614.

Bracci E, Centonze D, Bernardi G & Calabresi P (2002). Dopamine excites fast-spiking interneurons in the striatum. *J Neurophysiol* **87**, 2190–2194.

Bracci E, Centonze D, Bernardi G & Calabresi P (2003). Voltage-dependent membrane potential oscillations of rat striatal fast-spiking interneurons. *J Physiol* **549**, 121–130.

Calabresi P, Maj R, Pisani A, Mercuri NB & Bernardi G (1992). Long-term synaptic depression in the striatum: physiological and pharmacological characterization. *J Neurosci* **12**, 4224–4233.

Chang HT & Kita H (1992). Interneurons in the rat striatum: relationships between parvalbumin neurons and cholinergic neurons. *Brain Res* **574**, 307–311.

Destexhe A & Rudolph M (2004). Extracting information from the power spectrum of synaptic noise. *J Comput Neurosci* **17**, 327–345.

Ding JB, Guzman JN, Peterson JD, Goldberg JA & Surmeier DJ (2010). Thalamic gating of corticostriatal signaling by cholinergic interneurons. *Neuron* **67**, 294–307.

Dommett E, Coizet V, Blaha CD, Martindale J, Lefebvre V, Walton N, Mayhew JE, Overton PG & Redgrave P (2005). How visual stimuli activate dopaminergic neurons at short latency. *Science* **307**, 1476–1479.

Dringenberg HC, Vanderwolf CH & Noseworthy PA (2003). Superior colliculus stimulation enhances neocortical serotonin release and electrocorticographic activation in the urethane-anesthetized rat. *Brain Res* **964**, 31–41.

El Boustani S, Marre O, Behuret S, Baudot P, Yger P, Bal T, Destexhe A & Fregnac Y (2009). Network-state modulation of power-law frequency-scaling in visual cortical neurons. *PLoS Comput Biol* **5**, e1000519.

Fino E, Deniau JM & Venance L (2008). Cell-specific spike-timing-dependent plasticity in GABAergic and cholinergic interneurons in corticostriatal rat brain slices. *J Physiol* **586**, 265–282.

Gage GJ, Stoetzner CR, Wiltschko AB & Berke JD (2010). Selective activation of striatal fast-spiking interneurons during choice execution. *Neuron* **67**, 466–479.

Gittis AH, Nelson AB, Thwin MT, Palop JJ & Kreitzer AC (2010). Distinct roles of GABAergic interneurons in the regulation of striatal output pathways. *J Neurosci* **30**, 2223–2234.

Golomb D, Donner K, Shacham L, Shlosberg D, Amitai Y & Hansel D (2007). Mechanisms of firing patterns in fast-spiking cortical interneurons. *PLoS Comput Biol* **3**, e156.

Gruber AJ, Powell EM & O'Donnell P (2009). Cortically activated interneurons shape spatial aspects of cortico-accumbens processing. *J Neurophysiol* **101**, 1876–1882.

Hjorth J, Blackwell KT & Kotaleski JH (2009). Gap junctions between striatal fast-spiking interneurons regulate spiking activity and synchronization as a function of cortical activity. *J Neurosci* **29**, 5276–5286.

Holt GR, Softky WR, Koch C & Douglas RJ (1996). Comparison of discharge variability in vitro and in vivo in cat visual cortex neurons. *J Neurophysiol* **75**, 1806–1814.

Horikawa K & Armstrong WE (1988). A versatile means of intracellular labeling: Injection of biocytin and its detection with avidin conjugates. *J Neurosci Methods* **25**, 1–11.

Hutcheon B & Yarom Y (2000). Resonance, oscillation and the intrinsic frequency preferences of neurons. *Trends Neurosci* **23**, 216–222.

Kasanetz F, Riquelme LA, O'Donnell P & Murer MG (2006). Turning off cortical ensembles stops striatal Up states and elicits phase perturbations in cortical and striatal slow oscillations in rat in vivo. *J Physiol* **577**, 97–113.

Kawaguchi Y (1993). Physiological, morphological, and histochemical characterization of three classes of interneurons in rat neostriatum. *J Neurosci* **13**, 4908–4923.

Koos T & Tepper JM (1999). Inhibitory control of neostriatal projection neurons by GABAergic interneurons. *Nat Neurosci* **2**, 467–472.

Kremkow J, Aertsen A & Kumar A (2010). Gating of signal propagation in spiking neural networks by balanced and correlated excitation and inhibition. *J Neurosci* **30**, 15760–15768.

Mahon S, Deniau JM & Charpier S (2001). Relationship between EEG potentials and intracellular activity of striatal and cortico-striatal neurons: an in vivo study under different anesthetics. *Cereb Cortex* **11**, 360–373.

Mallet N, Le Moine C, Charpier S & Gonon F (2005). Feedforward inhibition of projection neurons by fast-spiking GABA interneurons in the rat striatum in vivo. *J Neurosci* **25**, 3857–3869.

Norenberg A, Hu H, Vida I, Bartos M & Jonas P (2010). Distinct nonuniform cable properties optimize rapid and efficient activation of fast-spiking GABAergic interneurons. *Proc Natl Acad Sci U S A* **107**, 894–899.

Oorschot DE (1996). Total number of neurons in the neostriatal, pallidal, subthalamic, and substantia nigral nuclei of the rat basal ganglia: a stereological study using the Cavalieri and optical disector methods. *J Comp Neurol* **366**, 580–599.

Pike FG, Goddard RS, Suckling JM, Ganter P, Kasthuri N & Paulsen O (2000). Distinct frequency preferences of different types of rat hippocampal neurones in response to oscillatory input currents. *J Physiol* **529**, 205–213.

Pitcher TL, Wickens JR & Reynolds JNJ (2007). Differences in striatal spiny neuron action potentials between the spontaneously hypertensive and Wistar-Kyoto rat strains. *Neuroscience* **146**, 135–142.

Planert H, Szydlowski SN, Hjorth JJ, Grillner S & Silberberg G (2010). Dynamics of synaptic transmission between fast-spiking interneurons and striatal projection neurons of the direct and indirect pathways. *J Neurosci* **30**, 3499–3507.

Plenz D & Kitai ST (1998). Up and down states in striatal medium spiny neurons simultaneously recorded with spontaneous activity in fast-spiking interneurons studied in cortex-striatum-substantia nigra organotypic cultures. *J Neurosci* **18**, 266–283.

Popescu AT, Popa D & Pare D (2009). Coherent gamma oscillations couple the amygdala and striatum during learning. *Nat Neurosci* **12**, 801–807.

Pouille F & Scanziani M (2001). Enforcement of temporal fidelity in pyramidal cells by somatic feed-forward inhibition. *Science* **293**, 1159–1163.

Ramanathan S, Hanley JJ, Deniau JM & Bolam JP (2002). Synaptic convergence of motor and somatosensory cortical afferents onto GABAergic interneurons in the rat striatum. *J Neurosci* **22**, 8158–8169.

Reynolds JNJ & Wickens JR (2000). Substantia nigra dopamine regulates synaptic plasticity and membrane potential fluctuations in the rat neostriatum, in vivo. *Neuroscience* **99**, 199–203.

Schulz JM, Oswald MJ & Reynolds JNJ (2011). Visual-induced excitation leads to firing pauses in striatal cholinergic interneurons. *J Neurosci* (in press).

Schulz JM, Redgrave P, Mehring C, Aertsen A, Clements KM, Wickens JR & Reynolds JNJ (2009). Short-latency activation of striatal spiny neurons via subcortical visual pathways. *J Neurosci* **29**, 6336–6347.

Schulz JM, Redgrave P & Reynolds JNJ (2010). Cortico-striatal spike-timing dependent plasticity after activation of subcortical pathways. *Front Synaptic Neurosci* **2**, 23.

Sharott A, Moll CKE, Engler G, Denker M, Grun S & Engel AK (2009). Different subtypes of striatal neurons are selectively modulated by cortical oscillations. *J Neurosci* **29**, 4571–4585.

Tepper JM, Tecuapetla F, Koós T & Ibáñez-Sandoval O (2010). Heterogeneity and diversity of striatal GABAergic interneurons. *Front Neuroanat* **4**, 150.

Tort ABL, Kramer MA, Thorn C, Gibson DJ, Kubota Y, Graybiel AM & Kopell NJ (2008). Dynamic cross-frequency couplings of local field potential oscillations in rat striatum and hippocampus during performance of a T-maze task. *Proc Natl Acad Sci U S A* **105**, 20517–20522.

Tseng KY, Kasanetz F, Kargieman L, Riquelme LA & Murer MG (2001). Cortical slow oscillatory activity is reflected in the membrane potential and spike trains of striatal neurons in rats with chronic nigrostriatal lesions. *J Neurosci* **21**, 6430–6439.

Tunstall MJ, Oorschot DE, Kean A & Wickens JR (2002). Inhibitory interactions between spiny projection neurons in the rat striatum. *J Neurophysiol* **88**, 1263–1269.

Wang XJ (2010). Neurophysiological and computational principles of cortical rhythms in cognition. *Physiol Rev* **90**, 1195–1268.

Wilson CJ, Chang HT & Kitai ST (1983). Disfacilitation and long-lasting inhibition of neostriatal neurons in the rat. *Exp Brain Res* **51**, 227–235.

Wonders CP & Anderson SA (2006). The origin and specification of cortical interneurons. *Nat Rev Neurosci* **7**, 687–696.

Acknowledgements

This work was supported by the Marsden Fund of the Royal Society of New Zealand (J.R.), Fellowships and a project grant from the Neurological Foundation of New Zealand (J.R., T.P. and M.O.), and a fellowship from the Health Research Council (J.W.). J.S. received a University of Otago Postgraduate Scholarship and Publishing Bursary.